Applied Magnetic Resonance
https://doi.org/10.1007/s00723-022-01499-3

Applied
Magnetic Resonance

ORIGINAL PAPER

Broadband Fourier-Transform-Detected EPR at W-Band

Manoj Vinayaka Hanabe Subramanya[1,2] · Jonathan Marbey[1,2,3] · Krishnendu Kundu[1] · Johannes E. McKay[1] · Stephen Hill[1,2]

Received: 31 May 2022 / Revised: 5 August 2022 / Accepted: 12 September 2022

Abstract

We report a true wideband Fourier transform (FT) EPR detection capability at the uniquely high frequency of 94 GHz (W-band). It is based on the quasi-optical HiPER spectrometer developed at the University of St. Andrews, into which we have integrated an arbitrary waveform generator (AWG) that is used to modulate the output from a solid-state multiplier chain prior to amplification, generating up to 1 kW microwave power with 1 GHz instantaneous bandwidth. Benchmark experiments are presented for a standard TEMPOL radical, which comprises a 500 MHz broad EPR spectrum at W-band. Using a single adiabatic chirp pulse, efficient inversion of this spectrum is demonstrated, enabling frequency-dependent studies of the longitudinal magnetization recovery in the time-domain, again via chirp pulse echo detection. From these measurements, an anisotropy in the spin–lattice relaxation time, T_1, can be determined with ease for TEMPOL. In addition, we implement the FT detection scheme for multi-dimensional (electron–electron double resonance, or ELDOR) experiments, demonstrating the full capabilities of the HiPER spectrometer. As an example, we present a chirp pulse, FT-detected version of the ELDOR NMR technique for the TEMPOL radical.

1 Introduction

Modern pulsed EPR spectroscopy is often performed at high magnetic fields and frequencies, as it can offer superior spectral resolution [1–3], sensitivity [4, 5], and orientation selectivity for anisotropic spin systems [6, 7]. Until recently, technological limitations associated with commercially available microwave components typically limited high-frequency EPR (HFEPR) experiments to narrow excitation bandwidths

---

✉ Stephen Hill
shill@magnet.fsu.edu

[1] National High Magnetic Field Laboratory, Tallahassee, Florida, USA

[2] Department of Physics, Florida State University, Tallahassee, Florida, USA

[3] Laboratory of Physical Sciences, University of Maryland, College Park, Maryland, USA

that are orders of magnitude smaller than the linewidths observed in commonly studied spectra. Thus, wideband measurements were performed in a time-consuming manner, where the applied magnetic field or frequency was progressively iterated in small steps [8]. By contrast, NMR spectroscopists began to utilize Fourier transform (FT) techniques in the 1960s to overcome similar limitations in the radio-frequency range [9], thereby mostly avoiding the limited bandwidth problem except in cases of quadrupolar nuclei [10, 11]. In particular, the advent of arbitrary waveform generators (AWGs) in the early 1990s largely eliminated the bandwidth problem in NMR [12, 13]. Gradually, this technology has matured to a point where AWGs may be employed as universal signal sources that provide complete amplitude and phase control over a given bandwidth, and at ever increasing frequencies, to the extent that commercially available devices now extend into the microwave regime [14, 15]. Consequently, these agile signal generators now provide a platform to perform FT-detected EPR [16–18], particularly at the widely used X-band frequency where high-power wideband amplifiers needed for pulsed studies are readily available due to their widespread use in telecommunications. The most popular applications have involved the generation of frequency-swept pulses for wideband inversion in dipolar spectroscopies such as double electron–electron resonance (DEER) [19, 20] and efficient saturation in dynamic nuclear polarization (DNP) schemes [21–23]. Up to now, broadband FT EPR detection has been limited to Q-band (34 GHz) [24].

The development of a quasi-optical pulsed EPR spectrometer (HiPER) at the University of St. Andrews utilizing a high-power extended interaction klystron (EIK) amplifier capable of delivering peak powers exceeding 1 kW, with an instantaneous bandwidth of 1 GHz, opened the door to true FT HFEPR at W-band (94 GHz) [25, 26]. Here, we report the integration of an AWG capability into a clone of the HiPER spectrometer installed at the US National High Magnetic Field Laboratory (NHMFL) in 2015; a detailed technical description of the spectrometer can be found in Ref. [25]. To demonstrate implementation of the AWG, we describe various pulsed HFEPR experiments utilizing the FT detection method on a dilute sample of the TEMPOL radical.

2 Theory of Adiabatic Pulses

The most widely employed approach to broadband FT EPR is based on the application of frequency-swept chirp pulses. This section briefly discusses the characteristics of such pulses [27, 28], which are defined by associated adiabaticity parameters. In modern electronics, adiabatic pulses are experimentally executed via time-dependent amplitude and phase modulation. However, the underlying principles and resultant effects on a given spin vector are best understood in a frequency modulated (FM) reference frame [29], also known as the rotating frame. The microwave magnetic field, $B_1(t)$, which is confined to the (xy-) plane perpendicular to the applied static B_0-field ($//z$), then undergoes amplitude and phase modulation, with the latter referenced to a fixed axis defined by the center frequency, ω_0, associated with the chirp. At time, t, the microwave B_1-field in the FM frame can be expressed as:

$$B_1(t) = \gamma_e^{-1}\omega_1(t)\exp[i\phi(t)t], \tag{1}$$

with $\omega_1(t)$ (in angular units) and $\phi(t)$ being the time-dependent microwave amplitude and phase, respectively; γ_e is the electron gyromagnetic ratio. If one further defines $\Delta\omega(t)$ as the frequency difference between the instantaneous microwave frequency $\omega(t)$ and the center frequency, ω_0, so that $\Delta\omega(t) = \omega(t) - \omega_0$, then $\Delta\omega(t)$ is related to the accumulated phase by the following integral:

$$\phi(t) = \int_{-\frac{1}{2}t_p}^{t} \Delta\omega\left(t'\right)dt', \tag{2}$$

with t_p being the pulse duration, while t is the time referenced to the center of the pulse, which lies within the interval $[-\frac{1}{2}t_p, +\frac{1}{2}t_p]$. The combination of Eqs. (1) and (2) and the time dependence of $\Delta\omega(t)$ completely define the chirp pulse. Depending on the nature of the frequency sweep, chirped pulses can be defined in variety of ways [27].

To obtain the experimental results, later described in Sect. 4, we have employed chirped pulses with a wideband, uniform rate, smooth truncation (WURST) windowing function [30]. A WURST pulse is characterized by a frequency sweep that is linear in t, and a time-dependent sine function that smoothly modulates the amplitude of the rising and falling edges of the pulse (Fig. 1a). Therefore, the chirp rate in a WURST pulse can be defined as $k = \omega_{sw}/t_p$, with ω_{sw} being the total sweep width. With these constraints, and in the context of Eq. (1), a WURST pulse is most generally defined by:

$$\omega_1(t) = \omega_{\mathrm{Max}}\left[1 - \left|\sin\left(\pi t/t_p\right)\right|^N\right] \tag{3}$$

and

$$\Delta\omega(t) = kt, \tag{4}$$

where ω_{Max} is the maximum amplitude. The shape of WURST pulses can vary significantly according to the user-specified exponent N: small N largely truncates the total bandwidth of the pulse, while $N > 50$ is desirable for smooth raising and falling edges without losing too much bandwidth (see Fig. 1a).

Given the above description of the microwave magnetic field associated with a chirped pulse, we can now describe the necessary conditions to achieve adiabaticity. The vector sum in Eq. (5) represents an effective time-dependent magnetic field during a chirp pulse in the rotating frame:

$$\vec{B}_{\mathrm{eff}}(t) = \gamma_e^{-1}\left[\omega_1(t) + \Delta\omega(t)\right], \tag{5}$$

where the experimental geometry constrains the direction of $\overrightarrow{\Delta\omega}$ along the $\pm z$-axis, parallel to the applied static magnetic field $\vec{B}_0$, while $\vec{\omega}_1$ is fixed along the x-axis. The magnitude is then given by $\left|B_{\mathbf{eff}}(t)\right| = \gamma_e^{-1}\sqrt{\left\{\omega_1(t)\right\}^2 + \{\Delta\omega(t)\}^2}$.

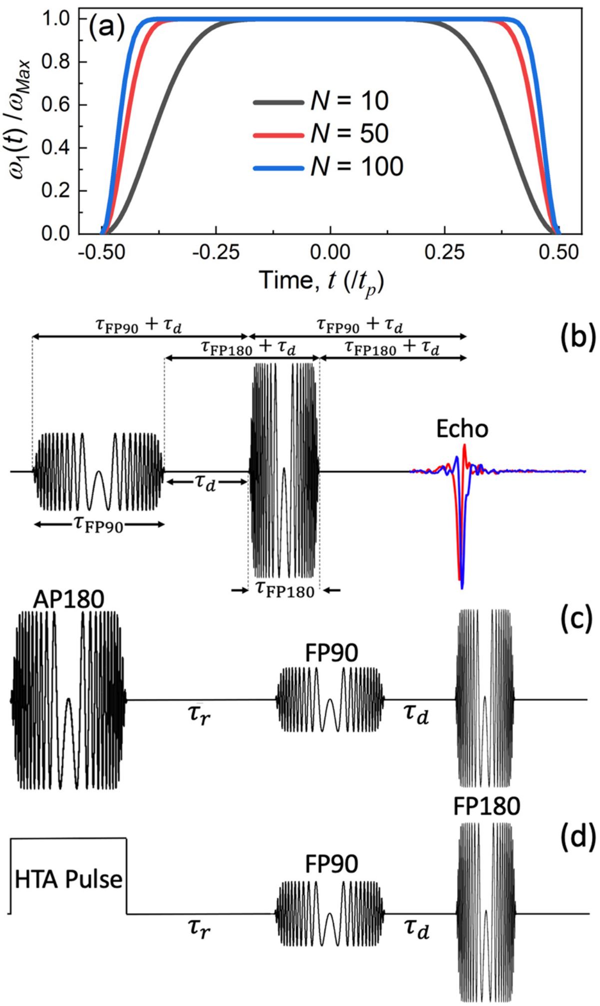

Fig. 1 **a** Amplitude profiles, $\omega_1(t)$, for the WURST pulse, with different values of N [Eq. (3)]. **b** Bodenhausen spin echo sequence with WURST pulses [$B_1(t)$ given by Eq. (1)], with the excitation pulse (FP90) being twice long as the refocusing pulse (FP180); a typical quadrature-detected chirped echo of TEMPOL is shown in blue (I) and red (Q). **c** Inversion recovery pulse sequence, where the spectrum is first inverted with an adiabatic π-pulse (AP180), followed by a Bodenhausen detection sequence. **d** CHEESY-detected NMR pulse sequence, where the AP180 pulse in (**c**) is replaced with a high-turning angle (HTA) saturating pulse. The horizontal axes are not to scale in (**c**, **d**)

According to Eq. (5), if $\Delta\omega$ starts positive and ends negative, the effective field $\vec{B}_{\mathrm{eff}}$ flips orientation from $+z$ to $-z$. In the context of chirped pulses, the adiabaticity condition requires the spin vector to follow $\vec{B}_{eff}(t)$ at all times during the sweep. To satisfy this condition, the rate of change of the orientation of $\vec{B}_{\mathrm{eff}}$ must be very slow compared to the spin nutation frequency. This implies that the adiabatic condition can be expressed as,

$$\frac{d\theta(t)}{dt} \ll \gamma_e B_{\mathrm{eff}}, \tag{6}$$

with $\theta(t)$ being the instantaneous tip angle of $\vec{B}_{\mathrm{eff}}$ away from the z-axis ($\pi/2$ for $\Delta\omega = 0$), and $\tan[\theta(t)] = \omega_1(t)/\Delta\omega(t)$. From this relation, the dimensionless adiabaticity factor, $Q(t)$, can be defined by the ratio

$$Q(t) = \frac{\gamma_e B_{\mathrm{eff}}}{d\theta(t)/dt}. \tag{7}$$

In the case of a WURST pulse (linear frequency sweep), $Q(t)$ can be expressed as [31]:

$$Q(t) = \frac{\left(k^2t^2 + \omega_1^2\right)^{3/2}}{k\omega_1}. \tag{8}$$

$Q(t)$ is minimum at the center of the chirp pulse, i.e., $\Delta\omega = 0$. This leads to an expression for the minimum, Q_{min}, as:

$$Q_{\mathrm{min}} = \frac{\omega_1^2}{k} = \frac{\omega_1^2 t_p}{\omega_{sw}} = \frac{2\pi\nu_1^2 t_p}{\nu_{sw}}. \tag{9}$$

Thus, Eq. (9) provides guidelines for achieving adiabaticity in terms of the choice of pulse length, t_p, microwave power, ν_1, and sweep width, ν_{sw} (expressed here in frequency units). For adiabatic inversion, $Q_{\mathrm{min}} \geq 5$ is recommended [32]. Otherwise, for an echo sequence where inversion is not required, excitation pulses are executed non-adiabatically, with Q_{min} well below unity.

3 Materials and Methods

3.1 AWG Implementation

A schematic diagram outlining integration of the AWG (Model M8190A, Keysight, Santa Rosa, CA, USA) into the NHMFL HiPER spectrometer is shown in Fig. 2. Overall, this is a relatively simple modification to the original transceiver (capable of generating monochromatic square pulses at two frequencies, with pulse-to-pulse phase cycling [25]). To generate an arbitrary waveform centered at 94 GHz, a 7.68333 GHz local oscillator (LO) is upconverted via a ×12 multiplier chain (QuinStar Technologies, Torrence, CA, USA) to 92.2 GHz. This is then harmonically mixed with the direct output from the AWG, centered at 1.8 GHz. The steady frequency of 7.68333 GHz is generated by a phase-locked permanent magnet yttrium iron garnet (YIG) tuned oscillator (Micro Lambda Wireless, Inc., Fremont, CA, USA). For FT HFEPR, the AWG is programmed to supply a pulsed waveform centered at 1.8 GHz with a sweepable frequency offset width of $\delta = \pm 500$ MHz. Such a scheme yields a resultant output frequency in the range of 94 ± 0.5 GHz. It

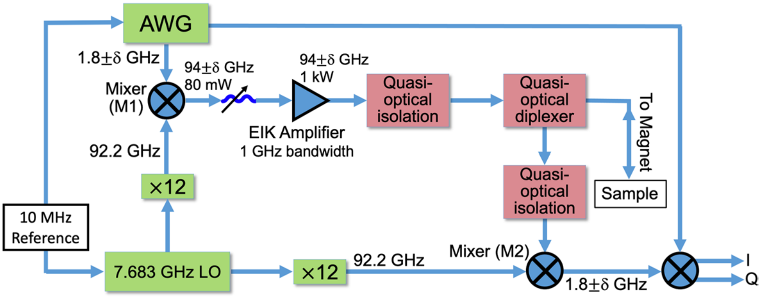

Fig. 2 A schematic of the AWG implementation in the W-band HiPER spectrometer; see main text for further explanation

is also possible to choose any frequency between 93.5 and 94.5 GHz as the center frequency and adjust the sweep range accordingly. The AWG and LO are further synchronized to a 10 MHz clock such that they remain phase coherent from shot to shot. The resultant waveform is further amplified to a maximum of 1 kW via the EIK amplifier (50 dB gain, VKB2475 series, Communications and Power Industries, Canada Inc.).

The output from the amplifier and the input to the receiver/detector are matched to free space via corrugated feed horns. In between, a corrugated waveguide probe (similarly matched to free space) couples the transmit signal to the sample and the resultant emission from the sample back to the receiver. Inductive mode detection enables excellent isolation of the cross-polar sample emission from the incident signal by means of a quasi-optical diplexer, providing low deadtime. Further details of the spectrometer are given in Ref. [25]. The achievable spectrometer bandwidth is ultimately limited by the profile of the amplifier, which quickly rolls off outside the 93.5 to 94.5 GHz range. On the detection side, the broadband emission centered at 94 GHz follows a two-step down-conversion scheme, first mixing out the 92.2 GHz signal generated by the ×12 LO, followed by an intermediate frequency (IF) of 1.8 GHz from the 2nd output channel of the AWG. This down-conversion scheme conveniently yields a final signal that possesses the exact same bandwidth, 2δ, that was initially generated by the AWG. During the second step of the down conversion, the reference signal is split and phase shifted by 90° for simultaneous in-phase (I) and quadrature (Q) detection. These signals are then digitized using a transient recorder (ADQ14DC-2X-PCIe, Teledyne, Thousand Oaks, CA) operating at a sampling rate of 2 GSa/s. According to Nyquist's theorem [33], this sampling rate is sufficient to cover the bandwidth of the EIK.

3.2 Flattening of the EIK Amplifier Profile

For the vast majority of pulsed EPR experiments, it is desirable to achieve uniform excitation over the available bandwidth, i.e., a uniform nutation frequency across the accessible spectrum. This requires a frequency-independent power, ν_1, arriving at the sample. In general, the nutation profile is given by a convolution of the frequency

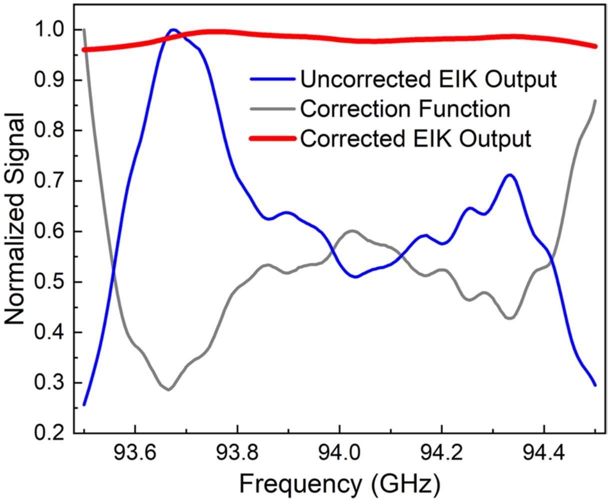

Fig. 3 Uncorrected EIK output power in the 93.5–94.5 GHz frequency range, together with the correction function that is used to obtain an approximately frequency-independent (flat) corrected EIK output; all curves are normalized to their maximum values

responses of the microwave amplifier, the microwave beam transport system (the quasi-optics in this case) and any resonator. To maximize bandwidth, HiPER does not employ a resonator [25]. Consequently, the quasi-optical design gives a relatively flat frequency profile and any corrections associated with the narrow-band response of a typical resonator [24, 32] can be avoided. However, the power profile, $P(\nu)$, of the EIK amplifier employed at the NHMFL currently has a 400% variation over its bandwidth (Fig. 3); note that this can vary over the lifetime of the amplifier. Taking advantage of the AWG, the nonuniformity can be compensated directly by careful manipulation of the input function. $P(\nu)$ can of course be determined experimentally using a known sample. As an obvious first guess, we use the reciprocal of $P(\nu)$ to rescale the AWG output and re-record the resultant $P'(\nu)$. However, due to nonlinearities associated with the amplifier and the mixer (M1 in Fig. 2), four to five iterations are generally needed to further correct the AWG output before a reasonably flat nutation profile is obtained, as seen in Fig. 3. The final amplitude profile is then obtained by multiplying the power correction function with, e.g., the desired WURST amplitude modulation function.

3.3 Sample

4-Hydroxy TEMPO [TEMPOL, where TEMPO = (2,2,6,6-Tetramethylpiperidin-1-yl)oxyl] and dimethyl sulfoxide (DMSO) were purchased from Sigma–Aldrich. All the presented experimental spectra were recorded for a 0.25 mM solution of TEMPOL dissolved in a 50/50 (v/v%) mixture of water and DMSO which forms a glass upon freezing. Approximately 50 µl of the solution was loaded into a 3 mm outer-diameter, 28 mm long polytetrafluoroethylene (PTFE) tube, which fits into the non-resonant inductive mode sample holder described in Ref. [25]. A sample temperature of 50 K was chosen to ensure a short enough spin–lattice relaxation time, T_1 (~5 ms), to achieve good signal-to-noise via averaging on reasonable time scales. Temperature control was achieved using a CF1200 helium-flow cryostat combined a MercuryiTC temperature controller (both Oxford Instrument PLC, UK).

3.4 Pulse Sequences

The pulsed HFEPR experiments described in the following section were designed to demonstrate the feasibility of the broadband FT detection technique using HiPER. In this context, an appropriate benchmark is provided by a comparison of the FT-detected spectrum of TEMPOL with the more conventional echo-detected field-swept (EDFS) spectrum of the same radical. The latter was recorded at a fixed frequency of 94 GHz using a Hahn echo sequence described by $\pi/2 - \tau - \pi - \tau -$ echo [34], where the angles refer to the rectangular nutation pulses of length $\tau_{\pi/2} = 100\,\text{ns}$ and $\tau_\pi = 200\,\text{ns}$, with an inter-pulse delay, $\tau = 600\,\text{ns}$.

To obtain FT-detected spectra, we implemented the Bodenhausen pulse sequence to generate broadband echoes; this is illustrated in Fig. 1b [35, 36]. For these purposes, the excitation and refocusing pulses are performed non-adiabatically with a much faster sweep rate compared, e.g., to the case where an exact broadband inversion pulse is required. Conventionally, these are referred to as fast-passage (FP) pulses, which we label FP90 and FP180 for excitation ($\pi/2$) and refocusing (π), respectively [32]. However, in contrast to the standard Hahn echo sequence, FP180 must have half the duration of FP90 (Fig. 1b). This may be understood as follows. If the chirps are performed from low to high frequency, then the FP90 pulse will sequentially excite spins from the low- to high-frequency ends of the spectrum, likewise the refocusing FP180 pulse. Consequently, the inter-pulse delay for spins excited at the start of the pulses will be $\tau_{\text{FP90}} + \tau_d$, with the echo occurring at $2(\tau_{\text{FP90}} + \tau_d)$, where τ_d is defined here as the delay time between the end of the FP90 pulse and the start of the FP180 pulse (Fig. 1b). Similarly, the inter-pulse delay for spins excited at the ends of the pulses will be $\tau_d + \tau_{\text{FP180}}$; however, the echo will occur at time $\tau_{\text{FP90}} + (2 \times \text{delay}) = \tau_{\text{FP90}} + 2(\tau_d + \tau_{\text{FP180}})$ after the start of start of the FP90 pulse. Therefore, in order for the echoes to occur at the same point in time, the pulse durations must satisfy the following equality: $2\tau_{\text{FP90}} = \tau_{\text{FP90}} + 2\tau_{\text{FP180}}$, i.e., $\tau_{\text{FP90}} = 2\tau_{\text{FP180}}$. Because of the linear frequency sweep rate associated with the WURST sequence [Eq. (4)], similar reasoning applies to all spins in the spectrum, i.e., they will refocus at exactly the same point in time for a $\tau_{\text{FP90}} : \tau_{\text{FP180}}$ ratio of 2:1. Meanwhile, the pulse amplitudes are modulated according to the WURST windowing function (Eq. (3), see also Fig. 1a). A value of $N = 100$ was employed in the experiments reported here, giving an approximate 10% truncation of the rising and falling edges of the pulses. To compensate for this truncation, the full bandwidth of the WURST pulses should be at least 25% larger than that of the EPR spectrum of interest. Since the full TEMPOL spectrum spans approximately 500 MHz at W-band, a sweep range of 700 MHz was employed throughout. The remaining pulse parameters were then optimized from visual comparison of the FT and EDFS spectra (Sect. 4): τ_{FP90} was fixed at 700 ns, with corresponding $\nu_1^{\mathrm{FP90}} = 5.5$ MHz. According to Eq. (9), these values correspond to $Q_{\mathrm{min}} = 0.2$, which is well below the adiabatic condition. Determining the optimum relative amplitudes of the FP90 and FP180 pulses requires numerical simulation, because fast-passage chirp pulses do not produce a linear relationship between nutation angle and pulse amplitude; we note that a $\nu_1^{\mathrm{FP90}} : \nu_1^{\mathrm{FP180}}$ power ratio of 1:10 was employed in Ref. [36]. Finally, the EIK power correction function was applied to both pulses.

With the Bodenhausen sequence properly implemented, one can then perform a broadband experiment in a single shot that would normally require tedious iteration over many parameters. For example, TEMPOL exhibits a T_1 variation across its spectrum [37, 38]. A complete map of this variation spanning 500 MHz would require at least 10 separate measurements using rectangular pulses (assuming 50 MHz bandwidth). Likewise, a field-swept version of the experiment would obviously require varying the applied field across the spectrum. In an adiabatic inversion recovery experiment, a truly adiabatic pulse (AP180) is first applied to invert the entire EPR spectrum. The polarization recovery is then measured using the chirp echo sequence described in the previous paragraph as a function of relaxation delay time, τ_r, between the AP180 and FP90 pulses; the full sequence is shown in Fig. 1c. To achieve the adiabatic condition for the AP180 pulse, $Q_{\mathrm{min}} > 5$ [Eq. (9)], ν_1 was set to 16.5 MHz (determined from Rabi nutation measurements) and a $\tau_{\mathrm{AP180}} = 10$ µs was used, resulting in $Q_{\mathrm{min}} \approx 25$.

FT methods may also be utilized as alternatives to other multi-dimensional EPR techniques, such as electron–electron double resonance (ELDOR-) detected NMR [8, 39, 40], where frequency iteration is involved. The FT version of this sequence, named Chirp Echo Epr SpectroscopY (CHEESY-) detected NMR [24], is shown in Fig. 1d. For these purposes, a 10 µs high-turning angle (HTA) monochromatic pulse is first applied, saturating a very narrow portion of the spectrum, i.e., burning a hole [39]. The resultant EPR spectrum is then detected via the chirp echo sequence. As a control, a reference FT EPR spectrum is also recorded with the HTA pulse tuned outside the chirp bandwidth. A ratio of these spectra produces an image of the hole, along with sidebands due to forbidden electron-nuclear transitions (further details are given below).

4 Results and Discussion

4.1 FT-Detected HFEPR Spectrum of TEMPOL

As discussed above, the Bodenhausen sequence enables single-shot FT detection of the inhomogeneously broadened EPR spectrum of the TEMPOL radical in frozen solution, which spans almost 500 MHz at an applied field of 3.4 T. This spectrum is rich in features arising primarily from an anisotropic g-tensor and the hyperfine coupling to the $I = 1$ nuclear spin associated with ^{14}N (99.6% natural abundance) [41]; the oxygen and carbon atoms are predominantly non-magnetic, while longer-range hyperfine coupling to protons is not resolved in the one-dimensional spectrum (see

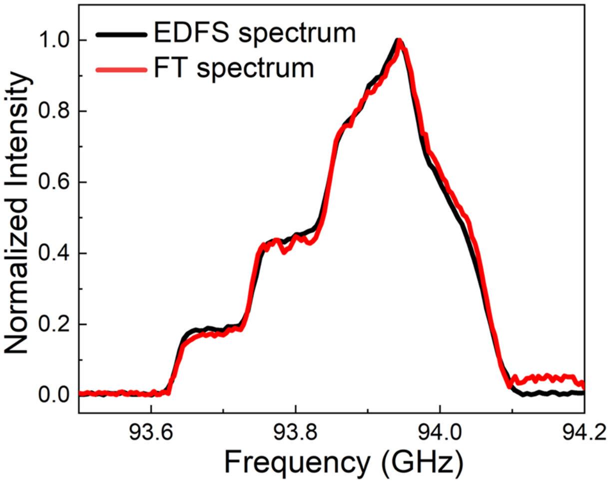

Fig. 4 Comparison of an echo-detected field-swept (EDFS) spectrum and a Fourier-transform-(FT-) detected spectrum for the same 0.25 mM TEMPOL sample at 50 K. The FT spectrum was acquired using the Bodenhausen sequence (Fig. 1b) at a magnetic field B_0=3.3445 T, with τ_{FP90} = 700 ns, τ_d = 600 ns, 20,000 averages and 33 Hz repetition rate. The EDFS spectrum, which employed narrow-band pulses of similar duration and 400 averages (100 Hz rep. rate) at each field step, has been transformed into the frequency domain

below). Figure 4 shows a direct overlay comparison between the FT and EDFS spectra, where the latter has been transformed into the frequency domain. The overall excellent match validates the use of an adiabatic factor, $Q_{\min} < 1$, for echo detection, as well as the EIK amplifier power flattening procedure.

4.2 Spin–Lattice and Spin–Spin Relaxation Time Measurements on TEMPOL

The results of wideband inversion recovery experiments are summarized in Fig. 5, which plots FT-detected spectra as a function of τ_r in (a) and (b). Immediately after the AP180 pulse, the spectrum is approximately inverted, i.e., it has a similar overall profile to the equilibrium spectrum observed at long times, albeit that the phase of the echo differs by π radians. The fact that the spectrum is not fully inverted for zero delay is most likely due to phase relaxation during the AP180 pulse (see also Fig. 6). At short delays, the inverted spectral intensity decays rapidly as a function of τ_r, passing through zero at ~1 ms, after which the equilibrium (positive) spectrum gradually recovers at longer delay times; note the log scale on the time axis in Fig. 5a, b, while a linear scale is employed in the inset to (c). The overall time dependence is characteristic of an exponential recovery of the echo amplitude of the form, $A(\tau, \nu) = A_0(\nu)\left\{1 - 2\exp\left(-\tau/T_1(\nu)\right)\right\}$, where τ denotes the relaxation delay time (τ_r) and $A_0(\nu)$ is the equilibrium echo amplitude. Interestingly, one sees from the false color map in Fig. 5b that different portions of the spectrum pass through zero at different delay times. This indicates that the longitudinal, or spin–lattice relaxation time, $T_1(\nu)$, depends strongly on frequency. In turn, this implies that T_1 is anisotropic,

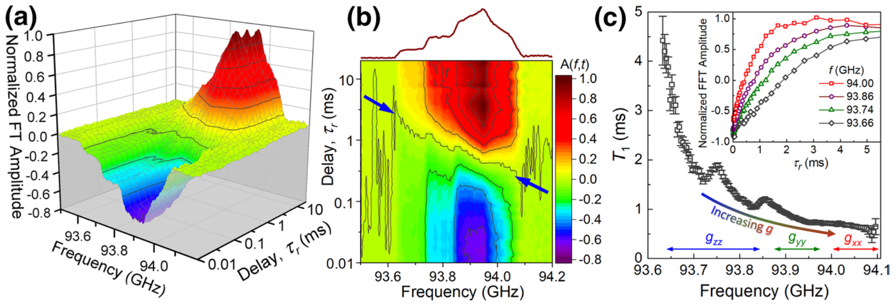

Fig. 5 **a** 3D plot of normalized 50 K FT spectra of a 0.25 mM TEMPOL sample as a function of relaxation delay time, τ_r, for the inversion recovery pulse sequence depicted in Fig. 1c; the magnetic field was set to $B_0 = 3.3445$ T, with $\tau_{\mathrm{AP180}} = 10$ µs, $\tau_{\mathrm{FP90}} = 700$ ns, $\tau_d = 600$ ns, 20,000 averages and 45 Hz repetition rate. **b** 2D false color map corresponding to the data in (**a**), with a representative long delay time spectrum shown at top. The blue arrows indicate the frequency-dependent delay times where the FT amplitude passes through zero. **c** Frequency- (or orientation-) dependence of the spin–lattice relaxation time, T_1, obtained by performing single exponential fits to the FT amplitude as a function of τ_r across the full spectrum; representative time traces are shown in the inset, and error bars represent the standard error associated with the exponential fits. A strong (~fivefold) variation in T_1 is observed for regions of the spectrum corresponding to different orientational components of the g-tensor (labeled at bottom)

because the different frequencies correspond to different g-values (Fig. 5c), thus reporting on TEMPOL molecules that are differently oriented with respect to the applied field (//z); note that, for TEMPOL, $\overleftrightarrow{g} = [2.0096, 2.0063, 2.0024]$ [41]. This behavior is further confirmed by fitting the recovery time traces to a single exponential function to obtain $T_1(\nu)$, as displayed in Fig. 5c. A fivefold increase is observed from high to low frequency.

In a separate experiment, FT-detected spectra were collected by varying τ_d (as defined in Fig. 1b) without the preceding AP180 pulse; the results are displayed in Fig. 6a. Exponential fits to the time traces provide a measure of the phase memory time, T_{m} (Fig. 6b). In contrast to T_1, no clear dependence on frequency is observed, i.e., there is no anisotropy associated with the phase memory time. T_1 relaxation in the solid-state is mediated by the interaction between the spins and the surrounding thermal bath [42]. In a quantum mechanical picture, this involves the interconversion of spin and vibrational energy quanta, mediated via spin–orbit coupling (SOC) present in the magnetic center or molecule [43, 44]. The strength of SOC in a spin-½ radical can be gauged by the deviation of the g-factor from the free electron value, $g_e = 2.0023$ [40]. As a result, spin–lattice relaxation should be more effective (shorter T_1) as the g-value deviates further from g_e, a trend that is clearly borne out in Fig. 5c. One also sees a slight dependence of T_1 for the different ^{14}N hyperfine components in the form of small inflections visible at each extremum. Such a dependence in TEMPOL has been reported in solutions [45]. However, the more likely explanation in the present case is again a variation of the actual (as opposed to effective) g-factor across each hyperfine component. Meanwhile, the phase memory time, T_{m}, is dominated by spin–spin interactions at low temperatures [46–48]. In dilute samples, it is primarily dynamics associated with the protons in the frozen matrix that cause dephasing. Such interactions are isotropic for radicals with weak

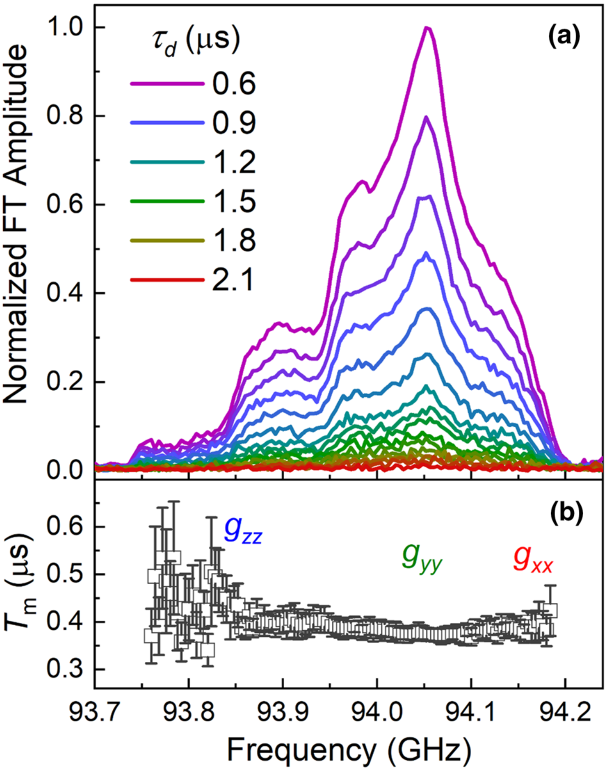

Fig. 6 **a** FT-detected EPR spectra of a 0.25 mM TEMPOL sample recorded at 50 K as a function of the delay between the FP90 and FP180 pulses in the Bodenhausen sequence (Fig. 1b), starting at $\tau_d = 600$ ns and increasing in 100 ns increments; the magnetic field was set to $B_0 = 3.3485$ T, with $\tau_{\text{FP90}} = 700$ ns, 20,000 averages and 50 Hz repetition rate. The echo intensity decreases with increasing delay because of dephasing. **b** The frequency- (or orientation-) dependence of the phase memory time, T_m, is obtained by performing single exponential fits to the FT amplitude as a function of τ_d across the spectrum; the error bars represent the standard error associated with the exponential fits

SOC anisotropy, in agreement with the experiments reported here. A more detailed discussion of these relaxation effects is beyond the scope of this study.

4.3 CHEESY-Detected NMR

CHEESY-detected NMR was originally performed by Wili et al. at Q-band (35 GHz) [24]. This multi-dimensional (pump-probe) technique is similar to conventional ELDOR-detected NMR [8]. In particular, both methods are capable of uncovering details of weak super-hyperfine interactions that are unresolved in one-dimensional spectra such as those in Figs. 4, 5 and 6. The reason is because the HTA pump pulse burns holes in the inhomogeneously broadened spectrum, thereby selecting narrower subsets of molecules in the distribution. In this case, the linewidth of the hole is determined either by the bandwidth of the HTA pulse or any intrinsic spin dynamics that contribute to homogeneous line broadening. Importantly, the residual linewidth is typically less than the spectral splitting caused by super-hyperfine interactions to more remote nuclei. Consequently, if the spectrum is subsequently imaged on timescales that are short in comparison to the spin–lattice or spectral diffusion lifetimes, one may resolve such super-hyperfine effects, which may be of immense diagnostic value, e.g., in biomolecular and biochemical structural investigations [49–51] or mechanistic studies of DNP [39, 52]. To do so using the conventional ELDOR technique, multiple experiments at variable observe frequencies are required. This may be time-consuming, particularly if the ELDOR spectrum spans a wide frequency range. On the other hand, CHEESY-detected NMR provides the entire spectrum in a single shot.

The detailed theory of CHEESY- [24] and ELDOR-detected NMR [8] can be found elsewhere. Both techniques rely on formally forbidden transitions involving simultaneous excitation of electron and nuclear spins (i.e., $\Delta m_s = \pm 1$, $\Delta m_I = \pm 1$) by the HTA pulse. The transition probability increases with increasing anisotropy in the relevant hyperfine interaction. Here, we consider the simplest possible case of an $S = ½$ radical and an $I = ½$ proton (^{1}H), coupled through space via the magnetic dipolar interaction, which is intrinsically anisotropic (the more complex $S = ½$, $I = 1$ case appropriate to ^{14} N is discussed in Ref. [8]). The inset to Fig. 7b depicts the corresponding energy diagram and the various allowed and weakly allowed transitions: single-quantum (SQ) electron spin resonance ($\Delta m_s = +1$ and $\Delta m_I = 0$), $\nu_{\mathrm{SQ}} = \gamma_e B_0 \pm \frac{1}{2}A$, where the ± refers to the state of the nuclear spin, γ_e is the electron gyromagnetic ratio in frequency units and A the hyperfine coupling strength (in general, A is orientation dependent [53]); zero quantum (ZQ) electron-nuclear resonance ($\Delta m_s = +1$ and $\Delta m_I = -1$), $\nu_{\mathrm{ZQ}} = \left(\gamma_e + \gamma_n\right) B_0$, where γ_n is the nuclear gyromagnetic ratio; and double quantum (DQ) electron-nuclear resonance ($\Delta m_s = +1$ and $\Delta m_I = +1$), $\nu_{\mathrm{DQ}} = \left(\gamma_e - \gamma_n\right) B_0$. In a CHEESY-NMR experiment, the FT-detected echo spectrum is dominated by the allowed SQ transitions. The deepest hole is observed at the same frequency as the HTA pulse because it saturates (bleaches) the corresponding SQ transitions at precisely that frequency. Meanwhile, the HTA pulse produces less pronounced holes due to excitation of the ZQ and DQ transitions. Likewise, this causes a bleaching of the FT-detected SQ spectrum. However, for ^{1}H, the positions of these holes are shifted with respect to the SQ hole by the following difference frequencies: $\Delta\nu = \nu_{\mathrm{SQ}} - \nu_{\mathrm{ZQ}}$ and $\Delta\nu = \nu_{\mathrm{SQ}} - \nu_{\mathrm{DQ}}$, i.e., $\Delta\nu = \pm\gamma_n B_0 \pm \frac{1}{2}A$. In other words, the ZQ/DQ holes occur on either side of the HTA reference (at $\Delta\nu = 0$), shifted by an amount corresponding to the NMR frequency, with an additional (often unresolved) splitting corresponding to the hyperfine interaction strength. Hence the name, CHEESY-detected NMR, because it yields an NMR spectrum that inherits EPR sensitivity and bandwidth. Here one sees a particular advantage of performing such experiments at high magnetic fields due to the corresponding high NMR frequencies, which enables better resolution of the ZQ/DQ signals from the central SQ intensity.

The result of a CHEESY-detected NMR experiment on TEMPOL is shown in Fig. 7b, with the horizontal scale referenced to the HTA pulse frequency (94.02 GHz). The final NMR spectrum is obtained by taking the difference between FT spectra recorded both with and without the HTA pulse. It has five main peaks

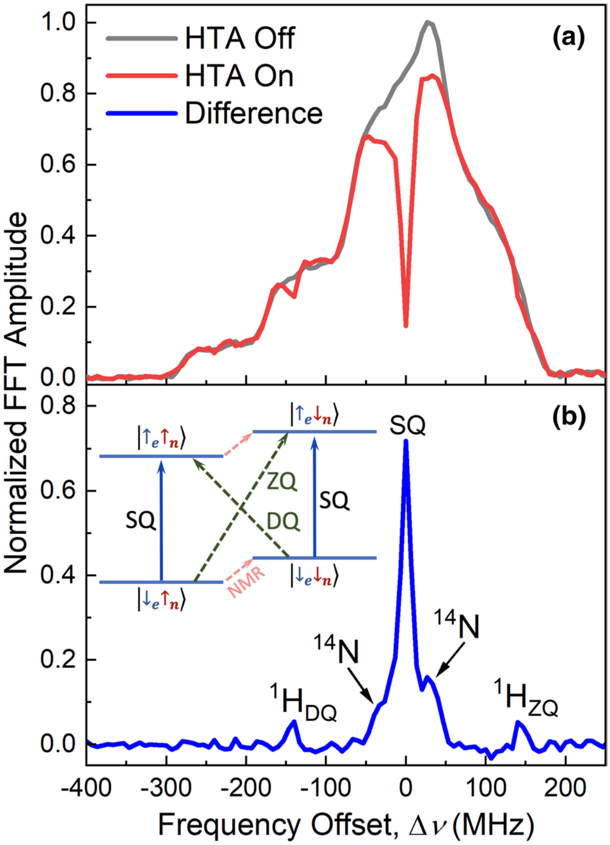

Fig. 7 **a** Comparison between FT spectra of a 0.25 mM TEMPOL sample recorded at 50 K using the CHEESY-detected NMR pulse sequence depicted in Fig. 1d, with the HTA pulse on and off; the magnetic field was set to $B_0 = 3.3485$ T, with $\tau_{\mathrm{FP90}} = 700$ ns, 20,000 averages and 25 Hz repetition rate; a 12 µs duration HTA pulse was employed, with a 10 µs delay to the FP90 pulse. **b** CHEESY-detected NMR spectrum obtained by taking the difference between the "off" and "on" spectra in (**a**), with the frequency referenced to the HTA pulse (94.02 GHz). The inset to **b** depicts the energy level diagram for the simple case of a hyperfine coupled $S = ½$, $I = ½$ electron-nuclear system (e.g., electron–^{1}H). The solid vertical lines denote SQ electron transitions, while the dashed green lines denote ZQ and DQ transitions. The ^{1}H$_{ZQ}$/^{1}H$_{DQ}$ and ^{14} N CHEESY-detected NMR signals are indicated in the main panel

including the central SQ transitions. The narrow ^{1}H peaks located symmetrically with respect to the central hole are easily identified, as they appear at the associated proton Larmor frequency ($\gamma_n B_0 = \pm 143$ MHz at 3.3485 T). Meanwhile, the two inner peaks can be assigned to ^{14} N present in the nitroxide moiety of the TEMPOL radical. In this case, due to the $I = 1$ nuclear spin and stronger hyperfine coupling, DQ and ZQ peaks occur either side of the central SQ hole. Moreover, in contrast to ^{1}H, their positions are dominated by the hyperfine interaction, with weaker shifts due to the ^{14} N nuclear Larmor frequency ($\gamma_n B_0 = \pm 10.4$ MHz at 3.3485 T). This results in broader peaks and a slight asymmetry with respect to the $\Delta\nu = 0$ position; for more in-depth discussion, see Refs. [8, 38].

5 Summary and Outlook

We demonstrate integration of an AWG capability into the broadband HiPER spectrometer operating at uniquely high W-band frequencies, facilitating multi-dimensional high-power FT EPR experiments. We benchmark this state-of-the-art spectrometer using the TEMPOL radical, demonstrating efficient adiabatic inversion of the entire 500 MHz wide spectrum, as well as hole-burning (pump–probe) experiments. This capability enables efficient studies of weak super-hyperfine electron-nuclear couplings and relaxation dynamics with the sensitivity and resolution inherent to high-field EPR. Beyond the benchmark experiments described in this work, the capabilities offered by chirped broadband pulsed EPR techniques are highly applicable to coherent population transfer in multi-level (i.e., $S > ½$) systems. Indeed, these techniques have already been demonstrated for Gd(III) spin labels in which the enhancement of the central transition was used to increase the sensitivity of dipolar-EPR measurements [54]. However, such techniques have yet to be applied to carefully oriented single crystals or in weakly exchange-coupled systems. Concerning further developments in the instrumentation, arbitrarily tailored pulse shaping can also be iteratively tuned via optimal control procedures. Such techniques are known to increase excitation efficiency by compensating for pulse distortions arising from *all* RF and quasi-optical components present in the spectrometer, including sample dependent geometries. Though optimally tailored pulses are commonly used in quantum information science applications, they are rarely employed in the context of pulsed EPR [55, 56]. As such, the techniques afforded by the addition of an AWG opens new possibilities in a range of research areas, from biomolecular structural studies and coordination chemistry to materials research and quantum spin sciences. Most notably, this capability resides at the US National High Magnetic Field Laboratory, where it is available to external users via a competitive proposal process.

Acknowledgements We are indebted to Rob Hunter, Paul Cruickshank, Graham Smith (St. Andrews University) for very fruitful advice and discussions, and Boris Epel (University of Chicago) for development of the software interface associated with the AWG-driven HiPER spectrometer.

Author Contributions SH, JM, and KK conceived the research. MVHS, JM, JEM, and KK carried out the AWG integration on the HiPER spectrometer. JEM designed and integrated the multiplier chain. MVHS and KK prepared the sample. SH, JM, MVHS, and KK designed the experiments, while MVHS and KK performed the measurements. MVHS and KK analyzed the EPR results. All authors contributed to the writing of the manuscript.

Funding This work was supported by the US Department of Energy (under DE-SC0020260 to SH). Work performed at the NHMFL is supported by the US National Science Foundation (DMR-1644779) and by the State of Florida.

Declarations

Conflict of interest The authors declare no competing financial interests.

References

1. S. Stoll, in *Electron Paramagnetic Resonance*, vol. 22, ed. by B.C. Gilbert, D.M. Murphy, V. Chechik (The Royal Society of Chemistry, Cambridge, UK, 2011), pp.107–154
2. C. Duboc-Toia, A.K. Hassan, E. Mulliez, S. Ollagnier-de Choudens, M. Fontecave, C. Leutwein, J. Heider, J. Am. Chem. Soc. **125**, 38 (2003). https://doi.org/10.1021/ja026690j
3. A. Savitsky, A.A. Dubinskii, H. Zimmermann, W. Lubitz, K. Möbius, J. Phys. Chem. B **115**, 11950 (2011). https://doi.org/10.1021/jp206841v
4. A. Savitsky, K. Möbius, Photosynth. Res. **102**, 311 (2009). https://doi.org/10.1007/s11120-009-9432-4
5. L. Motion, J.E. Lovett, S. Bell, S.L. Cassidy, P.A.S. Cruickshank, D.R. Bolton, R.I. Hunter, H. El Mkami, S. Van Doorslaer, G.M. Smith, J. Phys. Chem. Lett. **7**, 1411 (2016). https://doi.org/10.1021/acs.jpclett.6b00456
6. I. Kaminker, M. Florent, B. Epel, D. Goldfarb, J. Magn. Reson. **208**, 95 (2011). https://doi.org/10.1016/j.jmr.2010.10.010
7. P. Goldfarb, Chem. Chem. Phys. **8**, 2325 (2006). https://doi.org/10.1039/B601513C
8. D. Goldfarb, eMagRes **6**, 101 (2017). https://doi.org/10.1002/9780470034590.emrstm1516
9. R.R. Ernst, W.A. Anderson, Rev. Sci. Instrum. **37**, 93 (1966). https://doi.org/10.1063/1.1719961
10. A.J. Vega, eMagRes. (2010). https://doi.org/10.1002/9780470034590.emrstm0431.pub2
11. R.W. Schurko, eMagRes (2011). https://doi.org/10.1002/9780470034590.emrstm1199
12. I. Hung, A.R. Altenhof, R.W. Schurko, D.L. Bryce, O.H. Han, Z. Gan, Magn. Reson. Chem. **59**, 951 (2021). https://doi.org/10.1002/mrc.5128
13. R. Bhattacharyya, L. Frydman, J. Chem. Phys. **127**, 194503 (2007). https://doi.org/10.1063/1.2793783
14. G.G. Brown, B.C. Dian, K.O. Douglass, S.M. Geyer, B.H. Pate, J. Mol. Spectrosc. **238**, 200 (2006). https://doi.org/10.1016/j.jms.2006.05.003
15. C.B. Park, R.W. Field, J. Chem. Phys. **144**, 200901 (2016). https://doi.org/10.1063/1.4952762
16. M. Tseitlin, R.W. Quine, G.A. Rinard, S.S. Eaton, G.R. Eaton, J. Magn. Reson. **213**, 119 (2011). https://doi.org/10.1016/j.jmr.2011.09.024
17. T. Kaufmann, T.J. Keller, J.M. Franck, R.P. Barnes, S.J. Glaser, J.M. Martinis, S. Han, J. Magn. Reson. **235**, 95 (2013). https://doi.org/10.1016/j.jmr.2013.07.015
18. P.E. Spindler, S.J. Glaser, T.E. Skinner, T.F. Prisner, Angew. Chemie - Int. Ed. **52**, 3425 (2013). https://doi.org/10.1002/anie.201207777
19. P.E. Spindler, I. Waclawska, B. Endeward, J. Plackmeyer, C. Ziegler, T.F. Prisner, J. Phys. Chem. Lett. **6**, 4331 (2015). https://doi.org/10.1021/acs.jpclett.5b01933
20. T. Bahrenberg, Y. Rosenski, R. Carmieli, K. Zibzener, M. Qi, V. Frydman, A. Godt, D. Goldfarb, A. Feintuch, J. Magn. Reson. **283**, 1 (2017). https://doi.org/10.1016/j.jmr.2017.08.003
21. D. Breitgoff, K. Keller, M. Qi, D. Klose, M. Yulikov, A. Godt, G. Jeschke, J. Magn. Reson. **308**, 106560 (2019). https://doi.org/10.1016/j.jmr.2019.07.047
22. P.T. Judge, E.L. Sesti, N. Alaniva, E.P. Saliba, L.E. Price, C. Gao, T. Halbritter, S.T. Sigurdsson, G.B. Kyei, A.B. Barnes, J. Magn. Reson. **313**, 106702 (2020). https://doi.org/10.1016/j.jmr.2020.106702
23. I. Kaminker, R. Barnes, S. Han, J. Magn. Reson. **279**, 81 (2017). https://doi.org/10.1016/j.jmr.2017.04.016
24. N. Wili, G. Jeschke, J. Magn. Reson. **289**, 26 (2018). https://doi.org/10.1016/j.jmr.2018.02.001
25. P.A.S. Cruickshank, D.R. Bolton, D.A. Robertson, R.I. Hunter, R.J. Wylde, G.M. Smith, Rev. Sci. Instrum. **80**, 103102 (2009). https://doi.org/10.1063/1.3239402
26. T.V. Can, J.E. McKay, R.T. Weber, T. Dubroca, J. van Tol, S. Hill, R.G. Griffin, J. Phys. Chem. Lett. **9**, 3187 (2018). https://doi.org/10.1021/acs.jpclett.8b01002
27. R.A. De Graaf, eMagRes **5**, 1003 (2016). https://doi.org/10.1002/9780470034590.emrstm1443
28. L.A. O'Dell, Solid State Nucl. Magn. Reson. **55–56**, 28 (2013). https://doi.org/10.1016/j.ssnmr.2013.10.003
29. P.E. Spindler, P. Schöps, W. Kallies, S.J. Glaser, T.F. Prisner, J. Magn. Reson. **280**, 30 (2017). https://doi.org/10.1016/j.jmr.2017.02.023
30. Ē Kupče, R. Freeman, J. Magn. Reson. Ser. A **115**, 273 (1995). https://doi.org/10.1006/jmra.1995.1179
31. J. Baum, R. Tycko, A. Pines, Phys. Rev. A **32**, 3435 (1985). https://doi.org/10.1103/PhysRevA.32.3435
32. A. Doll, G. Jeschke, J. Magn. Reson. **246**, 18 (2014). https://doi.org/10.1016/j.jmr.2014.06.016
33. C.E. Shannon, Proc. IRE **37**, 10 (1949). https://doi.org/10.1109/JRPROC.1949.232969
34. L. Hahn, Phys. Rev. **80**, 580 (1950). https://doi.org/10.1103/PhysRev.80.580

35. M. Böhlen, I. Burghardt, M. Rey, G. Bodenhausen, J. Magn. Reson. **90**, 183 (1990). https://doi.org/10.1016/0022-2364(90)90377-L
36. M. Böhlen, M. Rey, G. Bodenhausen, J. Magn. Reson. **84**, 191 (1989). https://doi.org/10.1016/0022-2364(89)90018-8
37. E.M.M. Weber, H. Vezin, J.G. Kempf, G. Bodenhausen, D. Abergél, D. Kurzbach, Phys. Chem. Chem. Phys. **19**, 16087 (2017). https://doi.org/10.1039/C7CP03242K
38. M. Ramirez Cohen, A. Feintuch, D. Goldfarb, S. Vega, Magn. Reson. **1**, 45 (2020). https://doi.org/10.5194/mr-1-45-2020
39. X. Wang, J.E. McKay, B. Lama, J. van Tol, T. Li, K. Kirkpatrick, Z. Gan, S. Hill, J.R. Long, H.C. Dorn, Chem. Commun. **54**, 2425 (2018). https://doi.org/10.1039/C7CC09765D
40. S.M. Greer, J. McKay, K.M. Gramigna, C.M. Thomas, S.A. Stoian, S. Hill, Inorg. Chem. **57**, 5870 (2018). https://doi.org/10.1021/acs.inorgchem.8b00280
41. A.I. Smirnov, T.I. Smirnov, P.D. Morse, Biophys. J. **68**, 2350 (1995). https://doi.org/10.1016/S0006-3495(95)80417-0
42. H. Sato, V. Kathirvelu, G. Spagnol, S. Rajca, A. Rajca, S.S. Eaton, G.R. Eaton, J. Phys. Chem. B **112**, 2818 (2008). https://doi.org/10.1021/jp073600u
43. P. Kazmierczak, R. Mirzoyan, R.G. Hadt, J. Am. Chem. Soc. **143**(42), 17305 (2021). https://doi.org/10.1021/jacs.1c04605
44. G.C. Kragskow, C.D. Buch, J. Nehrkorn, M. Ozerov, S. Piligkos, S. Hill, N.F. Chilton, Nat. Commun. **13**, 825 (2022). https://doi.org/10.1038/s41467-022-28352-2
45. R. Biller, V.M. Meyer, H. Elajaili, G.M. Rosen, S.S. Eaton, G.R. Eaton, J. Magn. Reson. **225**, 52 (2012). https://doi.org/10.1016/j.jmr.2012.10.002
46. C. Chen, J.F. Hu, S. Stanton, H.-P. Hill, X.-G. Cheng, J. Phys. Chem. Lett. **11**, 2074 (2020). https://doi.org/10.1021/acs.jpclett.0c00193
47. E.R. Canarie, S.M. Jahn, S. Stoll, J. Phys. Chem. Lett. **11**, 3396 (2020). https://doi.org/10.1021/acs.jpclett.0c00768
48. J. Chen, S. Hoffman, K. Kundu, J. Marbey, D. Komijani, Y. Duan, A. Gaita-Ariño, X.-G. Zhang, S. Hill, H.-P. Cheng, arXiv:2106.05185 [quant-ph]. https://arxiv.org/abs/2106.05185
49. A. Collauto, S. Mishra, A. Litvinov, H.S. Mchaourab, D. Goldfarb, Structure **25**, 1264 (2017). https://doi.org/10.1016/j.str.2017.06.014
50. A. Giannoulis, A. Feintuch, Y. Barak, H. Mazal, S. Albeck, T. Unger, F. Yang, X.C. Su, D. Goldfarb, Proc. Natl. Acad. Sci. USA **117**, 395 (2020). https://doi.org/10.1073/pnas.1916030116
51. E. C. Kisgeropoulos, Y. J. Gan, S. M. Greer, J. M. Hazel, H. S. Shafaat, J. Am. Chem. Soc. **144**,11991 (2022). https://doi.org/10.1021/jacs.1c13738
52. Y. Hovav, I. Kaminker, D. Shimon, A. Feintuch, D. Goldfarb, S. Vega, Phys. Chem. Chem. Phys. **17**, 226 (2015). https://doi.org/10.1039/C4CP03825H
53. S. van Doorslaer, eMagRes **6**, 51 (2017). https://doi.org/10.1002/9780470034590.emrstm1517
54. A. Doll, M. Qi, N. Wili, S. Pribitzer, A. Godt, G. Jeschke, J. Magn. Reson. **259**, 153 (2015). https://doi.org/10.1016/j.jmr.2015.08.010
55. D.L. Goodwin, W.K. Myers, C.R. Timmel, I. Kuprov, J. Magn. Reson. **297**, 9 (2018). https://doi.org/10.1016/j.jmr.2018.09.009
56. P.E. Spindler, Y. Zhang, B. Endeward, N. Gershernzon, T.E. Skinner, S.J. Glaser, T.F. Prisner, J. Magn. Reson. **218**, 49 (2012). https://doi.org/10.1016/j.jmr.2012.02.013